Soil Dynamics and Earthquake Engineering 152 (2022) 107047

Contents lists available at ScienceDirect

Soil Dynamics and Earthquake Engineering

journal homepage: www.elsevier.com/locate/soildyn

Performance-based analysis of Transit tunnels in the Chilean subduction zone

Benjamín Lyon [a], Gabriel Candia [b,*], Carlos Gutiérrez [a], Jorge Macedo [c]

[a] Facultad de Ingeniería Civil Universidad del Desarrollo, Saantiago, Chile
[b] Facultad de Ingeniería Civil, Universidad del Desarrollo, and National Research Center for Integrated Natural Disaster Management (CIGIDEN), ANID/FONDAP/15110017, Santiago, Chile
[c] Geosystems Engineering, Georgia Institute of Technology, Atlanta, GA, USA

ARTICLE INFO

Keywords:
Shallow tunnels
Earthquakes
Subduction
Seismic hazard
Conditional scenario
Centrifuge experiments
Finite elements

ABSTRACT

In this article, we study the seismic response of a shallow metro tunnel in a subduction zone environment and the use of a performance-based approach to develop seismic demand hazard curves (SDHC) of key engineering demand parameters, such as drift ratio, surface settlement, bending moment, and axial loads. The tunnel consists of a 6-m diameter sprayed concrete lining in medium dense soil and is located in Santiago, Chile. To simulate its seismic response, a finite element model of the soil–tunnel system was implemented in OpenSees and validated against centrifuge test results, linear-equivalent solutions for a 1D soil column, and single elements in cyclic simple shear. The tunnel response was computed for 112 ground motions, selected and scaled using the conditional scenario approach. This approach assigns a rate of occurrence to each ground motion and therefore, allows for a direct computation of annual exceedance rates of the tunnel response parameters. For instance, at this specific location, the 2500-yr return period drift ratio in the lining is approximately 0.25% as a result of large deformations imposed by the surrounding soil. Likewise, axial loads between 0.3 and 1.0 MN/m and bending moments of ±0.2 MN•m/m are apparent from the axial load-moment interaction diagrams; these results are of great value for the design and verification of the tunnel based on the collapse or life-safety limit states. Notably, the current formulation relaxes the assumption of scaling ground motions to a particular intensity measure and can be a computationally efficient alternative to standard incremental dynamic analyses.

1. Introduction

Transit tunnels in shallow soil deposits can be damaged during an earthquake due to large ground deformations. Moreover, the presence of soft soils, liquefiable soils or other forms of ground failure increases the probability of a structural collapse, which could lead to loss of functionality of the tunnel network and its interdependent systems, as well as major indirect losses. For instance, the catastrophic failure of the Daikai metro station in the 1995 Kobe earthquake was the result of large horizontal forces imposed by the surrounding soils, consisting of very soft sandy silts and sands below the water table, with shear wave velocities less than 190 m/s [1].

Cases of poor tunnel performance during earthquakes generally involve rock failures [2], tunnels crossing active faults [3,4], liquefaction-induced damage [5–7], or slope failures affecting tunnel portals [7–9]. In contrast, tunnels built in competent soils subjected to strong shaking seem to perform very well, such as the tunnels in Santiago's metro network, which suffered no damage after the M_w 8.8 Chile earthquake of 2010. In addition, most case histories of tunnel response during earthquakes focus on shallow crustal seismicity (e.g. see Ref. [10] and references within), with only a few studies performed on subduction zone settings, e.g., Mayoral et al. [11] who studied the response of a shallow tunnel in stiff soil during the 2017 Puebla Mexico earthquake. In all cases, the limited number of well-documented case studies and the limitations of experimental models make the prediction of the tunnel response challenging, relying heavily on numerical modeling. In the current study, we use a performance-based approach to quantify the seismic demand on a shallow circular tunnel in medium dense sand and the results from a finite element implementation validated against centrifuge tests. Despite some limitations of centrifuge experiments to represent actual field conditions, this approach allows to evaluate the performance of a constitutive model before moving to a prototype scale.

* Corresponding author.
E-mail address: gcandia@udd.cl (G. Candia).

https://doi.org/10.1016/j.soildyn.2021.107047
Received 12 May 2021; Received in revised form 2 September 2021; Accepted 23 October 2021

A similar approach to validate numerical models with centrifuge experiments can be found in the literature (e.g. Refs. [12–15]).

The study concentrates on ground motions from subduction earthquakes, which can present distinctive characteristics compared to ground motions recordings from shallow crustal tectonic settings. For example, in evaluating seismically-induced slope displacements, Macedo et al. (2017) [16] and Bray et al. (2018) [17] highlighted that subduction type earthquakes have distinctive characteristics at long periods (in a response spectra representation), which ultimately influences the induced seismic displacements. Another salient difference is the longer duration of subduction type earthquakes (e.g. Ref. [18]), which can also influence the response of geotechnical systems (e.g., in liquefaction related problems). Thus, ground motions from subduction type earthquakes have their unique characteristics and have to be treated accordingly.

The study unit consists of a dual-track sprayed concrete tunnel 6 m in diameter with a crown depth of 12 m reinforced with triangular lattice girders, as shown in Fig. 1. The tunnel configuration used herein is commonly found in dense urban settings across subduction margins (e.g., South America, Mexico, and the Pacific Northwest); these critical facilities transport millions of passengers per day and are periodically affected by large megathrust earthquakes. Thus, the results herein should help engineers estimate engineering demand parameters for tunnels consistent with the design level prescribed in modern design codes. For this purpose, a hazard analysis based on the conditional scenario spectra approach (CSS) [19] is proposed, which resulted in a computationally efficient alternative to incrementally scaled ground motions. To our knowledge, this method has not been used for hazard assessment in shallow soil tunnels in subduction settings.

The following sections present a review of relevant numerical modeling studies, the finite element model developed as part of this study and its validation, a description of the hazard assessment methodology and its implementation, and the results of hazard-consistent engineering demand parameters (EDPs) developed for a tunnel in Santiago, Chile.

2. Literature review on numerical modeling of tunnels

Well-defined numerical models for tunnels are essential to understanding this complex soil-structure-interaction (SSI) problem. A vast body of literature has been devoted to modeling the seismic response of tunnels in dry sand (e.g. Refs. [20–25]) as well as tunnels in liquefiable media or below the water table (e.g. Refs. [26–28]). For example, in a numerical round robin test used to evaluate the seismic response of tunnels [22], five teams [29–33] performed independent full dynamic analyses to predict the centrifuge response of a circular tunnel in medium-dense sand [34]. The numerical models, implemented in state-of-the-art software, captured the acceleration of the sand layers reasonably well. However, because of fundamental differences in the constitutive laws, the shear strains and volumetric strains had considerable variation across models. In addition, the different assumptions in the soil-lining interface resulted in large differences in the internal lining forces when compared to the experimental results and closed-form solutions [35,36], particularly in the hoop forces. More recently, de Silva et al. [20] used the Mohr-Coulomb constitutive law and hysteretic damping to simulate the seismic response of shallow and deep tunnels in both loose and dense sand. The study used ten unscaled ground motions from shallow crustal settings to develop fragility functions for the demand-capacity ratio. The authors concluded that the tunnels mobilized approximately 30% of their strength and that the tunnels in loose sand are less vulnerable to strong shaking than tunnels in dense sand due to soil nonlinearity. Similar studies have analyzed the response of square tunnels [37,38] and the effects of volumetric changes resulting in significant surface settlement [23].

State-of-art numerical models can predict the soil-structure interaction reasonably well, giving us great insight into the seismic response of tunnels; however, most of the research has focused on numerical modeling aspects and not so much on hazard-consistent assessments under a performance-based framework, which is the focus of the current study.

Fig. 1. Sprayed concrete lining, lattice girders, and temporary excavation support. Metro Line 6, Santiago, Chile, 2014.

3. Numerical model of a circular tunnel in dry sand

The current research is based on a plain-strain finite element model of a circular tunnel implemented in OpenSees [39]. The tunnel is 6 m in diameter, has a sprayed concrete lining with a thickness of 0.3 m, and is built at a crown depth of 12 m, as shown in Fig. 2. The soil deposit is 60 m deep and 140 m wide, and the material is a uniform medium-dense Leighton Buzzard Sand (LBS) ($G_S = 2.65$, $e_{\min} = 0.613$, $e_{\max} = 1.014$ [40]) with a relative density $D_r = 75\%$ and underlain by an elastic halfspace of unit weight $\rho_s = 2.24\ \mathrm{kg/m^3}$, shear wave velocity $V_s = 760\ \mathrm{m/s}$ and compression wave velocity $V_p = 1420\ \mathrm{m/s}$. To ensure a free-field response on the lateral boundaries, two massive shear columns with equal displacement constraints are added on each side of the model. In addition, to simulate a quiet (absorbing) boundary the base nodes are attached to horizontal and vertical dashpots with damping coefficients $c_s = \rho_s V_s$ and $c_p = \rho_s V_p$, respectively. The ground motion was input as a distributed shear force $\tau_s = 2\rho_s V_s v_{su}$ along the base, where v_{su} is the particle velocity of the upward motion taken as one half of the outcrop motion's velocity [41].

The tunnel lining is modeled with 48 linear elastic beam elements with material properties $E = 30$ GPa (Young's modulus of sprayed concrete [42]) and mass density $\rho_l = 21.5\ \mathrm{kN/m^3}$. No-slip conditions are assumed for the lining-soil interaction. The soil deposit geometry is described with a mesh of 2134 four-node isoparametric elements with a maximum size $\Delta l < \lambda/10$, where $\lambda \approx 20$ m is the shortest wavelength considered in the analysis. The stress–strain relation of the sand is characterized with the multisurface plasticity relation PressureDependMultiyield [43] available in OpenSees, referred to herein as PDMY. This model uses a Drucker–Prager failure criterion, where the octahedral shear stress varies as a function of the octahedral shear strain γ and confining pressure p', as shown in Eq. (1). In this equation, γ_r is the shear strain corresponding to a 50% reduction in shear modulus, $G = G_r(p'/p'_r)^m$ is the pressure-dependent shear modulus, G_r is the low-strain shear modulus at a confining pressure $p'_r = 100$ kPa, and the exponent m controls the variation of the shear and bulk moduli with confining pressure.

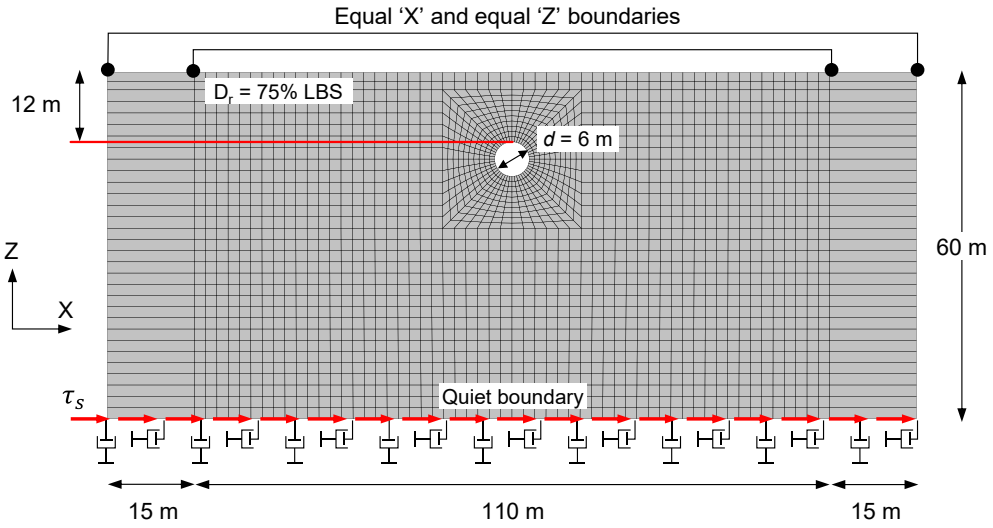

Fig. 2. Model geometry, finite element mesh, and boundary conditions.

$$\tau = \frac{G\gamma}{1 + \frac{\gamma}{\gamma_r}\left(\frac{p'}{p'_r}\right)^m} \quad (1)$$

Since no experimental data are available for this tunnel and soil deposit configuration, the calibration of the PMDY parameters is performed using a surrogate finite element model, which simulates the centrifuge response of a 6 m diameter tunnel in a 23.2-m deep deposit of LBS studied by Lanzano et al. (2012) [34] (refer to Model T3 and EQ (4) in Ref. [34]). The values of the 11 parameters required by the PMDY constitutive relation are summarized in Table 1; they include the mass density ρ_m, critical state friction angle φ_c (from TX-CD tests), and initial void ratio e_0 obtained from the laboratory tests on LBS reported by Visone & Santucci (2009) [40]. Additionally, the reference shear modulus G_r derives from resonant column torsional shear (RCTS) tests by Lanzano et al. (2014) [44], and the reference bulk modulus was computed from the relation $B_r = 2G_r(1 + \nu_m)/3(1 - 2\nu_m)$for linear-elastic materials assuming a Poisson's ratio of $\nu_m = 0.3$. The remaining parameters are based on the recommendations by Yang and Elgamal (2003) [43] for medium-dense sands.

The ground motions used in the centrifuge test consist of harmonic base excitations with amplitudes between 0.05 g and 0.15 g and frequencies between 0.375 Hz and 1 Hz (in prototype scale units). The finite element model and the calibrated PDMY parameters successfully reproduced the measured acceleration at several points throughout the soil deposit and adjacent to the tunnel [45]. For instance, a comparison of acceleration histories and 5% response spectra is shown in Fig. 3a and b for a point located at the free surface above the tunnel; in these figures, it is apparent that the finite element simulations capture the amplitude, phase and frequency content of the ground motion reasonably well. A similar response was observed for different control points across the model and different base acceleration inputs. Two additional tests were performed to validate the robustness of the selected PDMY parameters: (1) a single-element cyclic shearing test and (2) a shear wave amplification test. These tests are described briefly herein.

Table 1
Calibrated parameters for the constitutive relation PDMY.

Parameter	Value	Parameter	Value
Density, ρ_m	15.5 kN/m^3	Phase transformation angle, φ_{PT}	27°
Reference shear modulus, G_r	143 MPa	Contraction coefficient, c_t	0.05
Reference bulk modulus, B_r	310 MPa	Dilation coef. 1, di_1	0.6
Friction angle, φ_c	32°	Dilation coef. 3, di_3	3
Peak shear strain, γ_{max}	0.1	Initial void ratio, e_0	0.71
Mean pressure exponent, m	0.5		

We simulated a displacement-controlled simple-shear test in OpenSees to develop stress-strain hysteresis loops and then compared the resulting shear modulus reduction (G/G_{max}) and damping (D) curves with RCTS tests on LBS [40], as well as with other models available in the literature. As shown in Fig. 3c, the computed G/G_{max} values are in excellent agreement with the RCTS values and the median estimates as per Darandelli (2001) [46]. The damping ratios (Fig. 3d), on the other hand, are slightly higher than the RCTS values but in between Darandeli's [46] and Seed and Idriss's [47] damping ratios for dense sands. Finally, we tested the PDMY performance in reproducing the linear-equivalent response of a 23.2-m deep free-field soil deposit implemented in SHAKE, and compared the surface response against a fully nonlinear implementation in OpenSees. Both models were subjected to Kobe ground motion (PEER-RSN1104) scaled to PGA_{rock} values of 0.11 g and 0.05 g; as shown in Fig. 3e and f, the pseudoacceleration (Sa) spectra from the nonlinear and linear-equivalent models are in very good agreement, both at the short and long period ranges.

4. Seismic risk assessment methodology

In this study, we implemented a 4-step methodology to evaluate the site-specific seismic demand hazard curves (SDHC) for key tunnel response parameters (EDPs); the 4 steps are (1) site-specific PSHA analysis; (2) CSS-ground motion selection and scaling following the procedures in Arteta and Abrahamson [19]; (3) response history analysis; and (4) computation of SDHCs. A description of steps (1) through (4) is presented next.

STEP 1: Site-specific PSHA analysis

A probabilistic seismic hazard analysis (PSHA) is developed for the tunnel's location to produce the pseudoacceleration hazard curves and the conditional mean spectra (CMS) required later in step 2. The seismic hazard model must include the source geometry, magnitude recurrence laws, and rupture area scaling relations for all relevant seismic sources and tectonic settings. In addition, the PSHA model should account for epistemic uncertainty and the aleatory variability of the model parameters. For a model consisting of N_s seismic sources, the seismic hazard curve for the pseudoacceleration at period T_j is computed from the well-

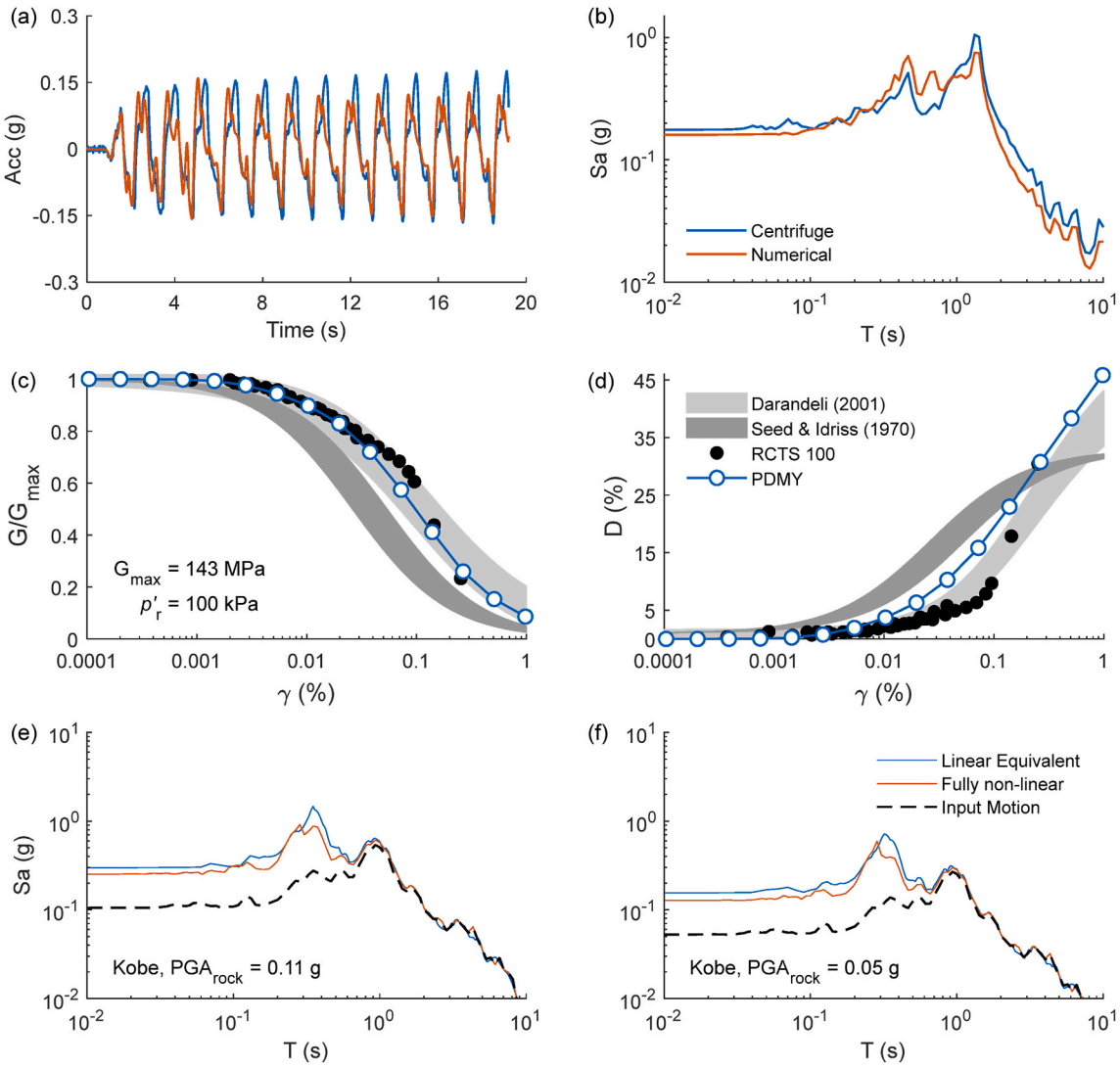

Fig. 3. PDMY validation results: (a) acceleration history at the free surface for a harmonic excitation and (b) the corresponding 5% response spectra. (c) Shear modulus reduction curves and (d) dumping amplification curves versus shear strain. Free field response for a 1D shear column for the Kobe ground motion scaled to (e) 0.11 g and (f) 0.05 g.

known PSHA equation. As an example, the PSHA equation can be written in its simplest form as

$$\lambda_{PSHA}(T_j,z)=\sum_{\ell=1}^{N_s}N^{\ell}(M_{min})\int_{M_{min}}^{M_{max}}\int_{0}^{R_{max}}P(Sa(T_j)>z|m,r)f_M^{\ell}(m)f_R^{\ell}(r,m)drdm \tag{2}$$

In Eq. (2), the term $N^{\ell}(M_{min})$ is the number of earthquakes with a magnitude above a magnitude threshold M_{min}, the term $P(Sa(T_j)>z|m,r)$ is the conditional probability that the pseudoacceleration $Sa(T_j)$ exceeds a level z, and the terms $f_M^{\ell}(m)$ and $f_R^{\ell}(r,m)$ are the probability density functions for magnitude and distance, respectively. For more details on the PSHA implementation, refer to Candia et al. (2019) [48].

In what follows and for the sake of notation simplicity, the subindex k refers to a variable at a hazard level k. For instance, if the k-th hazard level represents a mean annual rate of exceedance Λ, the notation X_k corresponds to the variable X consistent with the hazard level Λ. Thus, for a conditioning period T_0, the CMS and its variability at a hazard level k can be written as

$$CMS_k(T_j)=Sa(T_j|M_k,R_k)\exp(\rho(T_j,T_0)\varepsilon_k(T_0)\sigma(T_j)) \tag{3}$$

$$\sigma_{CMS,k}(T_j)=\sigma(T_j)\sqrt{1-\rho^2(T_j,T_0)} \tag{4}$$

where $Sa(T_j|M_k,R_k)$ and $\sigma(T_j)$ are the medium pseudoacceleration and standard deviation at period T_j obtained from a ground motion model (GMM). The terms M_k and R_k are the mean magnitude and distance obtained from a hazard deaggregation at the k-th hazard level, and $\rho(T_j,T_0)$ is the total correlation between the ground motion residuals at T_j and T_0. Finally, term $\varepsilon_k(T_0)$ is the number of log-standard deviations between $Sa_k(T_0)$ and the medium spectra $Sa(T_0|M_k,R_k)$, thus

$$\varepsilon_k(T_0)=\frac{\log Sa_k(T_0)-\log Sa(T_0|M_k,R_k)}{\sigma(T_0)} \tag{5}$$

Without loss of generality, in the current application, the terms $CMS_k(T_j)$ and $\sigma_{CMS,k}(T_j)$ are defined for a conditioning period $T_0=1\,s$ and structural periods $0.01\,s\le T_j\le 2\,s$. Additionally, ten hazard levels are considered (i.e., $k=1,\cdots,10$), corresponding to mean rates of exceedance of $\Lambda=\{0.1,\ 0.05,\ 0.025,\ 0.0126,\ 0.0063,\ 0.0032,\ 0.0016,\ 0.0008,\ 0.0004,\ 0.0002\}$ events/yr.

STEP 2: CSS ground motion selection

A set of nS ground motions that best represent the CMS and its variability are selected from a ground motion database using Monte Carlo simulations for each hazard level k. The best set is selected using a log-likelihood function, which is defined as:

$$LL_k = \sum_{i=1}^{nS}\sum_{j=1}^{nP} -\ln\left(\sigma_{CMS,k}(T_j)\right) - \frac{\left(\ln\left(\alpha_{i,k}Sa_i(T_j)\right) - \ln CMS_k(T_j)\right)^2}{2\sigma^2_{CMS,k}(T_j)} \quad (6)$$

where nP is the number of structural periods, $\alpha_{i,k}$ is the scaling factor applied to the i-th ground motion at the k-th hazard level, and $Sa_i(T_j)$ is the pseudoacceleration of the i-th ground motion at period T_j. The set with the best fit to the CMS and its variability (i.e., the set with maximum likelihood LL_k) is selected at each hazard level and scaled to the midpoint value between $Sa_k(T_0)$ and $Sa_{k+1}(T_0)$.

The i-th ground motions in the k-th hazard level is assigned an initial value of the rate of occurrence as defined in Eq. (7), where Λ_k and Λ_{k+1} are the hazard levels k and $k+1$, respectively.

$$\text{Rate}_{i,k} = \frac{\Lambda_k - \Lambda_{k+1}}{N} \quad (7)$$

This initial rate assignment can be used to build hazard curves for $Sa(T_j)$ by adding across the nS ground motions and the nH hazard levels the rates of ground motions that exceed the intensity level z, as shown in Eq. (8), where $\mathrm{H}(\cdot)$ is the step function.

$$\lambda_{CSS}(T_j, z) = \sum_{i=1}^{nS}\sum_{k=1}^{nH} \text{Rate}_{i,k}\mathrm{H}\left(\alpha_{i,k}Sa(T_j) - z\right) \quad (8)$$

To minimize the misfit between the PSHA-based hazard curves (Eq. (2)) and the CSS-recovered hazard curves (Eq. (8)), the rates of occurrence are adjusted iteratively using the penalty function in Eq. (9), where $\text{wt}(T_j)$ is a period-dependent weight to specify the range of periods on which a tight fit is desired. Using a simple grid search on the space of rate values, the penalty function is evaluated until a minimum value is obtained. Ground motions whose initial rate is reduced by a factor of 100 or more are removed from the subset, resulting in a total of $n_{CSS} \leq n_S n_H$ recordings.

$$\text{Penalty} = \sum_{j=1}^{nP}\sum_{k=1}^{nH} \text{wt}(T_j)\left(\ln\lambda_{\text{CSS}}(T_j, z_k) - \ln\lambda_{\text{PSHA}}(T_j, z_k)\right)^2 \quad (9)$$

The procedures outlined in step 2 produce a set of n_{CSS} acceleration time histories with their respective rate of occurrence and are readily useable for dynamic analyses.

STEP 3: Response History Analysis

The response of the soil-tunnel system to each of the ground motions defined in step 2 is obtained numerically by solving Eq. (10), where $\mathbf{u}$, $\dot{\mathbf{u}}$, and $\ddot{\mathbf{u}}$ are the absolute displacement, velocity and acceleration at each degree of freedom, respectively, $\mathbf{M}$ is the mass matrix, $\mathbf{F}_{nl}(\mathbf{u})$ is the vector of nonlinear internal forces, and $\mathbf{F}_{sw}$ are the self-weight forces. In addition to the energy dissipated by the stress-strain cycles on soil elements, 2% Rayleigh damping at $f_{min} = 3.2$ Hz was added for numerical stability and is represented by the damping matrix $\mathbf{C}$.

$$\mathbf{M}\ddot{\mathbf{u}} + \mathbf{C}\dot{\mathbf{u}} + \mathbf{F}_{nl}(\mathbf{u}) = \mathbf{F}_{sw} + \mathbf{F}(t) \quad (10)$$

Each ground motion is input as a shear stress $\tau_s = 2\rho V_{s_s} v_{st}$ distributed along the quiet boundary. This shear stress is converted to nodal forces and represented by the vector $\mathbf{F}(t)$ in Eq. (10). To initialize the stress field due to gravity, the self-weight is applied in a transient analysis with the soil modeled as an elastic material; once static equilibrium is reached, the soil constitutive relation is updated to its nonlinear formulation. The system's response history is obtained using a Newmark integration scheme ($\gamma = 0.5$, $\beta = 0.25$) and a constant time step $\Delta t = 0.005$ seg.

STEP 4: Computation of seismic demand hazard curves (SDHC)

The EDPs are retrieved from the response history analyses defined in step 3; they correspond to: (1) maximum axial loads (N) and maximum bending moments (M) on the lining, (2) dynamic increment of diametral strains (ε_d), (3) horizontal drift ratios (Δ), and (4) surface settlement above the tunnel (δ_z). The lining response parameters N, M and ε_d are defined as the maximum value of the parameter irrespective of the orientation; however, alternative EDP definitions are also possible. Using the CSS approach to risk assessment, SDHCs are obtained by adding the rates of the ground motions that result in EDPs in excess of a threshold value edp, i.e.,

$$\lambda_{CSS}(edp) = \sum_{i=1}^{nS}\sum_{k=1}^{nH} \text{Rate}_{i,k}\mathrm{H}\left(EDP_{i,k} - edp\right) \quad (11)$$

where $EDP_{i,k}$ represents a response parameter due to the i-th ground motion at the k-th hazard level. Note that Equations (8) and (11) have a similar structure; indeed, the rate of exceedance for any output variable can be evaluated in a similar fashion.

The computational bottleneck of this method lies in the solution of the equation of motion (Eq. (10)) in step 3; in this case, the runtime is proportional to n_{CSS}. An alternative method to build the SDHCs is to convolute the EDP fragility functions and the seismic hazard curve λ_{IM}, as shown in Eq. (12) [49], where N_{IM} is the number of sampling points of the hazard curve. At each ground motion level, the computation of the probability term requires the selection and scaling of n ground motions to a particular intensity measure (IM), with n being as large as 20, 30 or 100 (e.g. Refs. [50–52]) to accurately characterize the EDP distribution. Therefore, if $n_{CSS} \ll n \cdot N_{IM}$ a significant reduction of runtime can be achieved.

$$\lambda_{IDA}(EDP > edp) = \sum_{i=1}^{N_{IM}} P(EDP > edp | IM = im_i)\left|\Delta\lambda_{IM}(im_i)\right| \quad (12)$$

As discussed in the next section, the number ground motions resulting from the CSS approach in this example is $n_{CSS} = 112$. In contrast, implementing Eq. (12) using $N_{IM} = 10$ samples for the seismic hazard curve and $n = 20$ records per intensity level would yield 200 ground motion simulations, almost doubling the computational costs.

5. An illustrative example: hazard analysis for a tunnel in the chilean subduction zone

In the following example, consider the soil–tunnel system from Fig. 2 hypothetically located in Santiago, Central Chile, a region periodically affected by large subduction earthquakes. The objective here is to compute site-specific hazard curves for the internal lining forces, drift ratios, diametral strains, and surface settlement, following the proposed methodology. Details about the implementation and a discussion of the results are provided for each step.

5.1. Site-specific PSHA analysis

A seismic hazard model for a rock site ($V_{S30} = 760$ m/s) located in Santiago (33.4124°S; 70.5635°W) was implemented in SeismicHazard V3.0, a state-of-art PSHA software; see full documentation in Ref. [48]. The geometry of seismic sources, segmentation, and Guttenberg Richter parameters were obtained from Poulos et al., 2019 [53], which accounts for three interface sources with depths between 5 and 60 km and four intraslab sources at depths between 60 km and 160 km. The rupture area scaling with magnitude uses the median model by Strasser et al., 2010 [54], and the growth of rupture surfaces is constrained by the source geometry.

The ground shaking intensity at the tunnel site was obtained using the Montalva et al. (2017) [55] GMM for both interface and intraslab

sources. The seismic hazard at this location is presented in Fig. 4a and b in terms of uniform hazard spectra (UHSs) and conditional mean spectra (CMSs). A color code is used to identify the hazard levels, which range from $\Lambda_1 = 0.1$ events/yr (dark gray) to $\Lambda_{10} = 0.0002$ events/yr (light gray). The CMS calculation used the interperiod correlation model by Abrahamson et al., 2016 [56], which is valid for subduction environments. The dots in Fig. 4a and b correspond to the pseudoacceleration at the conditioning period, i.e., $Sa_k(T_0 = 1\ \mathrm{s})$, which defines the hazard level to each spectrum.

5.2. CSS ground motion selection

Candidate ground motions were selected from the SIBER-RISK database [57], which contains over 4600 ground motions, primarily from subduction interface and intraslab earthquakes recorded in Chile and south of Peru. The initial search criteria considered earthquakes with moment magnitudes $5 \leq M_w \leq 8.8$, recorded at a distance $R_{rup} <$ 1000 km at sites with 550 m/s $\leq V_{S30} \leq$ 900 m/s. The CSS ground motion selection procedure was performed in the 'Scenario Spectra Program' embedded in SeismicHazard V3.0. The set contains $n_{CSS} = 112$ acceleration records (from 18 earthquakes and 30 unique recordings) with their corresponding rates of occurrence and scaling factors; only the north-south component of each record was considered in the dynamic analysis. Specific details about the set are provided in Table A1, including the unique identifier for the event and ground motion, the initial and optimized rates, and scaling factors.

The 5% damped response spectra of the selected ground motions are shown in Fig. 5a, with a color scheme corresponding to the associated hazard level. The $Sa(T_j)$ hazard curves for different structural periods are shown in Fig. 5b. Note that the CSS-recovered hazard curves (dots) are in excellent agreement with the PSHA-based hazard curves (lines) for hazard levels considered.

5.3. Response history analysis

The solution to Eq. (10) for the ground motions defined in step 3 was implemented in OpenSees using a transient analysis. The magnitude of key response parameters was retrieved from the analysis results; their values are summarized in Table A2 and presented in Figs. 6–8 as a function of the peak ground acceleration of the outcropping motion ($PGA_{outcrop}$); in these figures, the color scale represents the hazard level of the corresponding input ground motion. In addition, the response parameters versus other IMs are presented in appendix figures A1 to A4.

Surface PGA values for a point located directly above the tunnel and a point located on the boundary (i.e., free-field conditions) are shown in Fig. 6a. It is apparent that PGA increases linearly for $PGA_{outcrop} < 0.4$ g and is de-amplified for $PGA_{outcrop} > 0.4$ g due to soil nonlinearity. This behavior is consistent with that of site class C1, according to the site classification system proposed by Seed et al. (1997) [58] (i.e., medium depth, stiff cohesionless soils). Seismically induced volumetric strains resulted in surface settlements up to 100 mm, as shown in Fig. 6b. Notice that the computed settlements above the tunnel are of the same order of magnitude as those in free-field conditions.

The lining distortions imposed by the surrounding soil are presented in Fig. 7a and b in terms of the maximum horizontal drift ratio and maximum diametral strains increment, respectively. A close inspection of the results shows that the drift ratios very closely match the free-field shear strains at the tunnel depth and that at this deformation level the sand undergoes a significant reduction in shear stiffness. The diametral strains ε_d reported in Fig. 7b are computed over all possible orientations; however, in agreement with [35,59], they mostly occur at angles of $\pm 45°$; these strains are approximately 20% lower than Wang's 1993 solution for perforated ground without lining [35].

The maximum axial load and maximum-minimum bending moments on the lining are shown in Fig. 8 and in Appendix figures A2-A3. These plots show that the internal forces increase with increasing ground shaking intensity, and that among the four IMs analyzed ($PGV_{outcrop}$, $PGA_{outcrop}$, and $Sa_{outcrop}$ at T = 0.5 and 1s), the variability on the internal forces against $PGV_{outcrop}$ is significantly lower. In addition, for $PGA_{outcrop}$ smaller than ~0.2 g the maximum bending moment is approximately constant and equal to its static component, i.e., the dynamic increment of bending moment is negligible.

The envelopes of M − P trajectories are shown in the interaction diagrams of Fig. 9 for two return periods: 625 yr and 2500 yr; as a reference, Fig. 9 also presents the yield surface of a 0.3-m thick lining reinforced with a triangular lattice girder ($1\varphi 28$ for positive moment and $2\varphi 22$ for negative moment). The histories of bending moment and axial load for the ground motions associated to a return period of 625 yr are shown in Figure A5; from these figures, it is apparent that the M − P trajectories trespass the yield surface on multiple instances, which could be indicative of severe structural damage.

5.4. Computation of EDPs hazard

The mean rate of exceedance of the different EDPs is obtained from Eq. (11), and the corresponding hazard curves are presented in Fig. 10. In these figures, the rates of exceedance range between 10^{-4} and 10^{-1} events/yr, which is consistent with the hazard levels represented in the ground motion dataset. Note that diametral strains hazard curve is similar in shape to the lining drift hazard curve but slightly shifted to the right. For a return period of 2500 yr, the lining deformation values are $\varepsilon_d = 0.27\%$ and $\Delta = 0.21\%$, which are indicative of significant soil nonlinearity. Likewise, the surface settlement and moment demand on the lining for a 2500 yr return period are $\delta_z = 60$ mm and $M =$

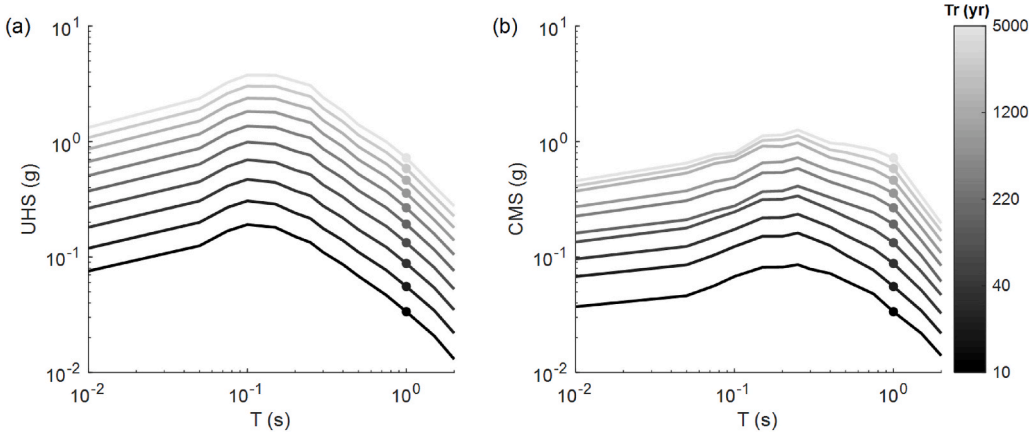

Fig. 4. (a) Uniform hazard spectra, and (b) conditional mean spectra; the color scale indicates the hazard level (return period) for each spectrum.

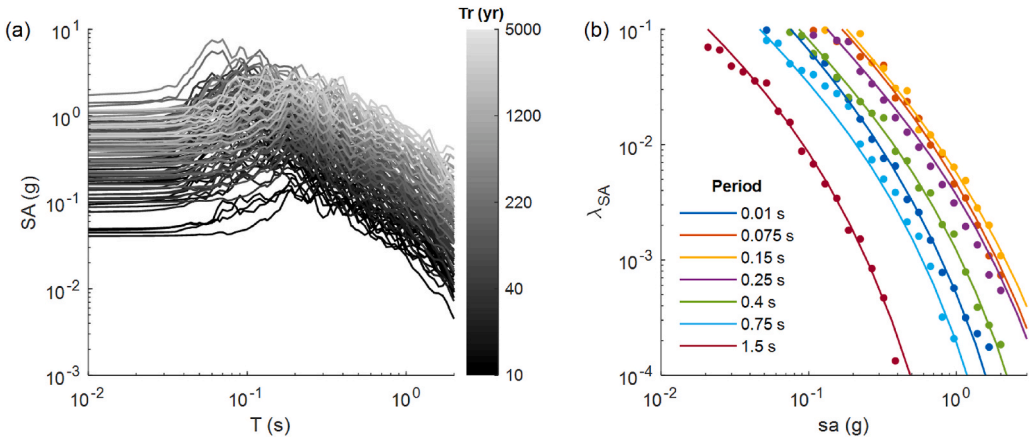

Fig. 5. (a) The 5% damped response spectra of selected ground motions, and (b) comparison of the PSHA-based (continuous lines) and CSS-recovered (dots) seismic hazard curves.

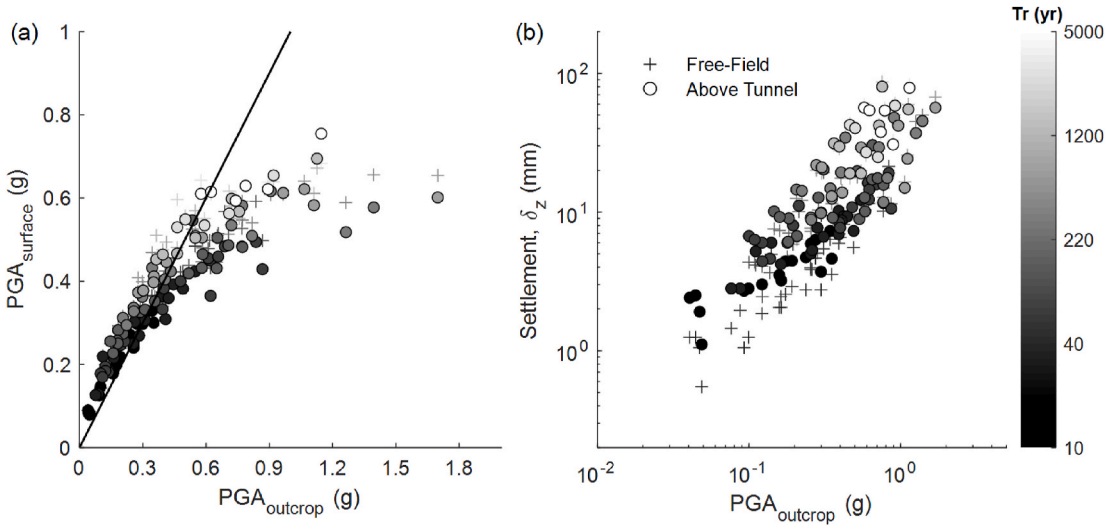

Fig. 6. (a) Surface PGA and (b) surface settlement, both above the tunnel and free-field.

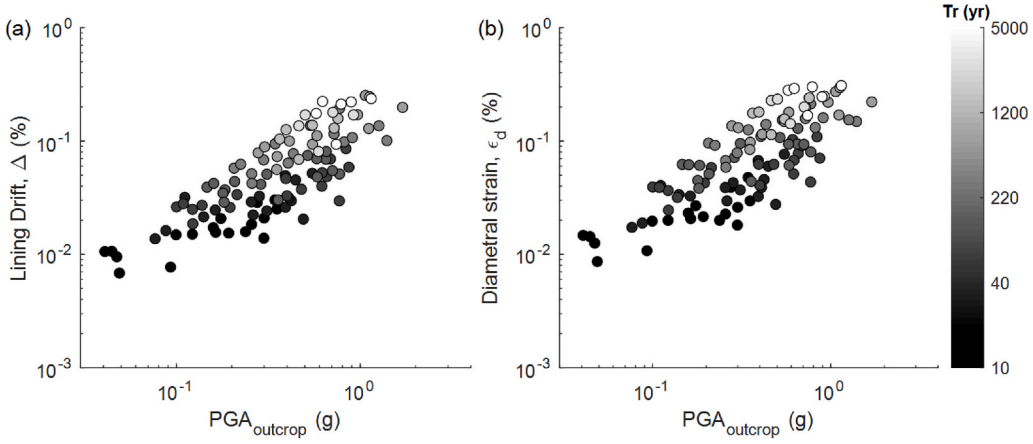

Fig. 7. Lining deformation measures: (a) drift ratios and (b) diametral strains.

0.2 MN·m/m, respectively. These response parameters should aid designers in verifying the performance objectives of modern seismic codes.

6. Conclusions

The current study evaluates the seismic response of a shallow circular tunnel in medium-dense soil using the conditional scenario spectra approach for ground motion scaling and hazard assessment. The main

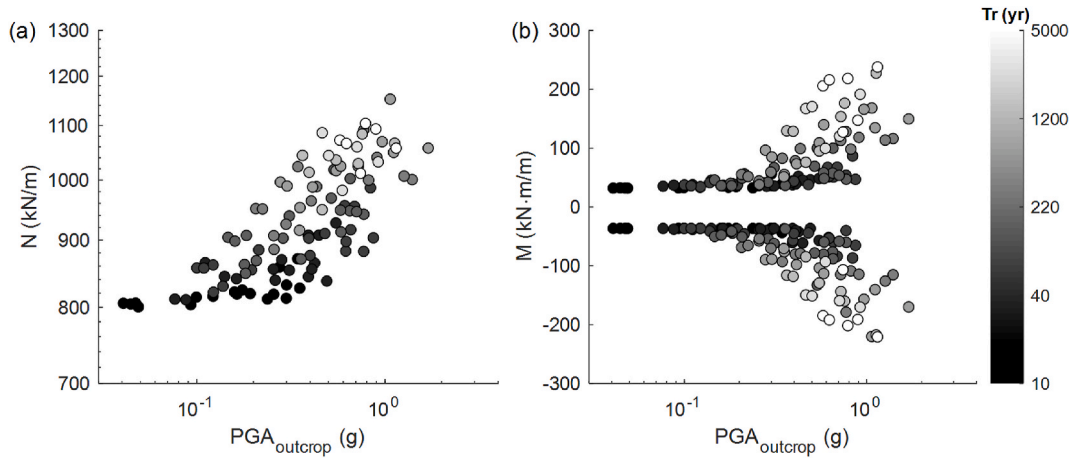

Fig. 8. Maximum values of (a) axial load and (b) bending moment on the lining; a positive moment corresponds to tension in the exterior fiber.

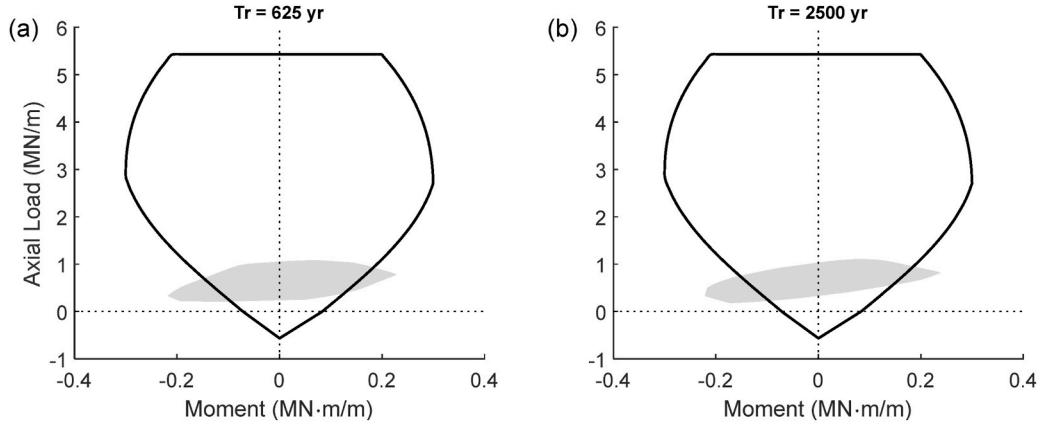

Fig. 9. Axial load–moment interaction diagram (gray patches) and yield surface (continuous lines) on the lining for two hazard levels: (a) 625 yr and (b) 2500 yr return period.

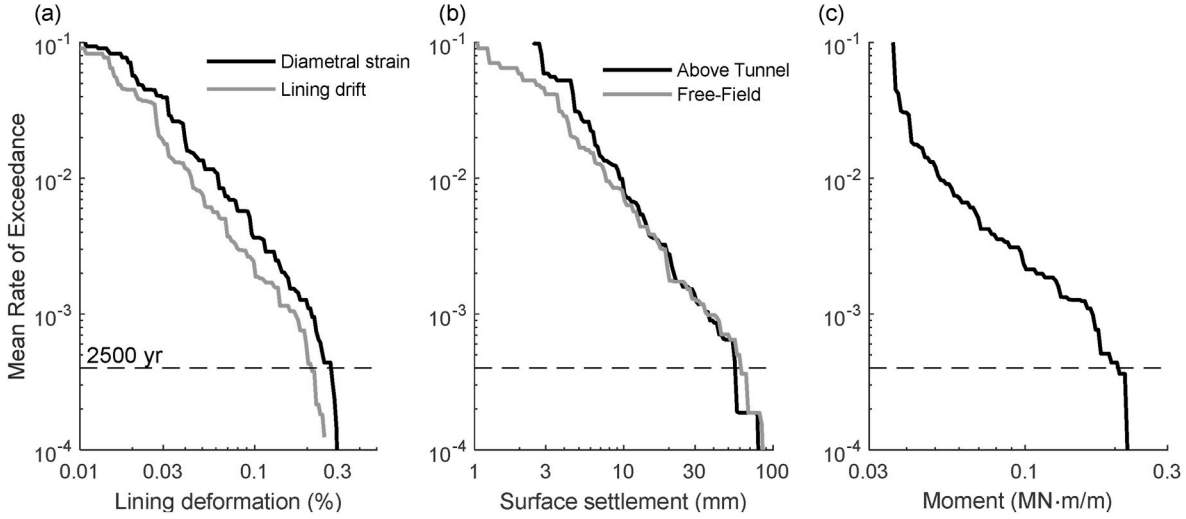

Fig. 10. EDP hazard curves of (a) drift ratios and diametral strains, (b) surface settlement, and (c) bending moment.

contribution from a geotechnical point of view consists of characterizing the tunnel response due to ground motions from a subduction zone and site-specific hazards. For this purpose, a 2D nonlinear finite element model was developed to simulate the soil-tunnel interactions due to ground accelerations. Validation for this numerical model was performed in three stages, including a comparison of (1) surface accelerations against centrifuge test results of a circular tunnel in dry sand, (2) G/G_{max} and damping curves against measured and published relations, and (3) free-field responses of a 1D soil column against a linear equivalent solution implemented in SHAKE.

The dynamic analysis in the soil-tunnel system considered a suite of 112 ground motions from the SIBER-RISK strong motion database [57]. The results were cast in terms seismic demand hazard curves (SDHC) of key response parameters, namely, lining internal forces, ground surface settlements, and lining distortion measures. The main advantages of this approach with respect to traditional incremental dynamic analyses, is that (1) each ground motion is assigned an occurrence rate which greatly simplified the computation of SDHCs, and (2) that the number of ground motions required to describe the SDHC can be significantly reduced. Most importantly, the scaling of ground motion used in the dynamic analyses is not biased toward a particular intensity parameter (e.g., PGA or the pseudo-acceleration at a particular period); in fact, in the current study the spectral ordinates in the period range 0–2 s and their cross-correlations are properly represented in the selected ground motions. The latter point partially solves an unsettled problem in geotechnical engineering regarding the selection of the most efficient intensity measure when analyzing buried structures. The risk-targeted response parameters obtained (e.g., axial load-moment diagrams in Fig. 9 or the drift hazard curves in Fig. 10) allow us to design and verify the tunnel lining based on the performance objectives specified in modern design codes.

CRediT authorship contribution statement

Benjamín Lyon: Writing – review & editing. **Gabriel Candia:** Conceptualization, Writing – review & editing. **Carlos Gutiérrez:** Writing – review & editing. **Jorge Macedo:** Conceptualization, Writing – review & editing.

Declaration of competing interest

The authors declare that they have no known competing financial interests or personal relationships that could have appeared to influence the work reported in this paper.

Acknowledgments

This research was sponsored by ANID/FONDECYT Grant N°11180937 “Seismic Risk of Mined Tunnels”, ANID/FONDECYT Grant N°1170836 “SIBER-RISK: SImulation Based Earthquake Risk and Resilience of Interdependent Systems and NetworKs”, the National Research Center for Integrated Natural Disaster Management (CIGIDEN) ANID/FONDAP/15110017, and Facultad de Ingeniería Civil at Universidad del Desarrollo. Dr. Macedo also acknowledges the financial support provided by the Civil and Environmental Engineering Department of the Georgia Institute of Technology. The authors are grateful for these supports and also acknowledge the two anonymous reviewers for their constructive comments.

Appendix A. Supplementary data

Supplementary data to this article can be found online at https://doi.org/10.1016/j.soildyn.2021.107047.

References

[1] Yoshida N. Damage to subway station during the 1995 Hyogoken-Nambu (Kobe) earthquake. In: Earthquake geotechnical case histories for performance-based design; 2009. p. 373–89.
[2] Stevenson JR, Kachali H, Whitman Z, Seville E, Vargo J, Wilson T. Preliminary observations of the impacts the 22 February Christchurch earthquake had on organisations and the economy. Bull N Z Soc Earthq Eng 2011;44(2):65–76. https://doi.org/10.5459/bnzsee.44.2.65-76.
[3] Yashiro K, Kojima Y, Shimizu M. Historical earthquake damage to tunnels in Japan and case studies of railway tunnels in the 2004 Niigataken-Chuetsu earthquake. Quarterly Report of RTRI 2007;48(3):136–41. https://doi.org/10.2219/rtriqr.48.136.
[4] Zhang X, Jiang Y, Sugimoto S. Seismic damage assessment of mountain tunnel: a case study on the Tawarayama tunnel due to the 2016 Kumamoto Earthquake. Tunn Undergr Space Technol 2018;71:138–48. https://doi.org/10.1016/j.tust.2017.07.019.
[5] Schmidt B, Hashash Y, Stimac T. “US Immersed Tube Retrofit” Tunnel and Tunnelling International Magazine. 1998. p. 22–4. November.
[6] Besharat V. The methods of remediation of existing underground structure against liquefaction. In: 15th Word Conference on earthquake engineering; 2012 [Lisbon].
[7] Yamazaki Y, Segawa N, Koizumi A. Evaluation of earthquake resistance of shield-tunnel/vertical-shaft connections and countermeasure technology. NTT Tech Rev 2013;11(1):1–6.
[8] Wang WL, Wang TT, Su JJ, Lin CH, Seng CR, Huang TH. Assessment of damage in mountain tunnels due to the Taiwan Chi-Chi earthquake. Tunn Undergr Space Technol 2001;16(3):133–50. https://doi.org/10.1016/S0886-7798(01)00047-5.
[9] Yu H, Chen J, Bobet A, Yuan Y. Damage observation and assessment of the Longxi tunnel during the Wenchuan earthquake. Tunn Undergr Space Technol 2016;54:102–16. https://doi.org/10.1016/j.tust.2016.02.008.
[10] Hashash YM, Hook JJ, Schmidt B, John I, Yao C. Seismic design and analysis of underground structures. Tunn Undergr Space Technol 2001;16(4):247–93. https://doi.org/10.1016/S0886-7798(01)00051-7.
[11] Mayoral JM, Mosqueda G, De La Rosa D, Alcaraz M. Tunnel performance during the Puebla-Mexico 19 september 2017 earthquake. Earthq Spectra 2020;36(2 suppl):288–313. https://doi.org/10.1177/8755293020976140.
[12] Bray JD, Macedo J. 6th Ishihara lecture: simplified procedure for estimating liquefaction-induced building settlement. Soil Dynam Earthq Eng 2017;102:215–31. https://doi.org/10.1016/j.soildyn.2017.08.026.
[13] Bullock Z, Karimi Z, Dashti S, Porter K, Liel AB, Franke KW. A physics-informed semi-empirical probabilistic model for the settlement of shallow-founded structures on liquefiable ground. Geotechnique 2019;69(5):406–19. https://doi.org/10.1680/jgeot.17.P.174.
[14] Karimi Z, Dashti S. Seismic performance of shallow founded structures on liquefiable ground: validation of numerical simulations using centrifuge experiments. J Geotech Geoenviron Eng 2016;142(6):04016011. https://doi.org/10.1061/(ASCE)GT.1943-5606.0001479.
[15] Manzari MT, El Ghoraiby M, Kutter BL, Zeghal M, Abdoun T, Arduino P, et al. Liquefaction experiment and analysis projects (LEAP): summary of observations from the planning phase. Soil Dynam Earthq Eng 2018;113:714–43. https://doi.org/10.1016/j.soildyn.2017.05.015.
[16] Macedo J, Bray J, Travasarou T. Simplified procedure for estimating seismic slope displacements in subduction zones. In: Proc., 16th World Conf. On earthquake engineering; 2017.
[17] Bray JD, Macedo J, Travasarou T. Simplified procedure for estimating seismic slope displacements for subduction zone earthquakes. J Geotech Geoenviron Eng 2018;144(3):04017124. https://doi.org/10.1061/(ASCE)GT.1943-5606.0001833.
[18] Macedo J, Liu C. Ground-motion intensity measure correlations on interface and intraslab subduction zone earthquakes using the NGA-sub database. Bull Seismol Soc Am 2021;111(3):1529–41. https://doi.org/10.1785/0120200297.
[19] Arteta CA, Abrahamson NA. Conditional scenario spectra (CSS) for hazard-consistent analysis of engineering systems. Earthq Spectra 2019;35(2):737–57. https://doi.org/10.1016/j.tust.2016.02.008.
[20] de Silva F, Fabozzi S, Nikitas N, Bilotta E, Fuentes R. Seismic vulnerability of circular tunnels in sand. Geotechnique 2021;1–15. https://doi.org/10.1680/jgeot.19.SiP.024.
[21] Huang ZK, Pitilakis K, Tsinidis G, Argyroudis S, Zhang DM. Seismic vulnerability of circular tunnels in soft soil deposits: the case of Shanghai metropolitan system. Tunn Undergr Space Technol 2020;98:103341. https://doi.org/10.1016/j.tust.2020.103341.
[22] Bilotta E, Lanzano G, Madabhushi SG, Silvestri F. A numerical Round Robin on tunnels under seismic actions. Acta Geotechnica 2014;9(4):563–79. https://doi.org/10.1007/s11440-014-0330-3.
[23] Kampas G, Knappett JA, Brown MJ, Anastasopoulos I, Nikitas N, Fuentes R. Implications of volume loss on the seismic response of tunnels in coarse-grained soils. Tunn Undergr Space Technol 2020;95:103127. https://doi.org/10.1016/j.tust.2019.103127.
[24] Cilingir U, Madabhushi SPG. A model study on the effects of input motion on the seismic behaviour of tunnels. Soil Dynam Earthq Eng 2011;31:452–62. https://doi.org/10.1016/j.soildyn.2010.10.004.
[25] Tsinidis G, Pitilakis K, Anagnostopoulos C. Circular tunnels in sand: dynamic response and efficiency of seismic analysis methods at extreme lining flexibilities. Bull Earthq Eng 2016;14(10):2903–29. https://doi.org/10.1007/s10518-016-9928-1.
[26] Liu H, Song E. Seismic response of large underground structures in liquefiable soils subjected to horizontal and vertical earthquake excitations. Comput Geotech 2005;32(4):223–44. https://doi.org/10.1016/j.compgeo.2005.02.002.
[27] Azadi M, Hosseini SMM. The uplifting behavior of shallow tunnels within the liquefiable soils under cyclic loadings. Tunn Undergr Space Technol 2010;25(2):158–67. https://doi.org/10.1016/j.tust.2009.10.004.
[28] Khoshnoudian F, Shahrour I. Numerical analysis of the seismic behavior of tunnels constructed in liquefiable soils. Soils Found 2002;42(6):1–8. https://doi.org/10.3208/sandf.42.6_1.
[29] Amorosi A, Boldini D, Falcone G. Numerical prediction of tunnel performance during centrifuge dynamic tests. Acta Geotechnica 2014;9(4):581–96. https://doi.org/10.1007/s11440-013-0295-7.
[30] Conti R, Viggiani GM, Perugini F. Numerical modelling of centrifuge dynamic tests of circular tunnels in dry sand. Acta Geotechnica 2014;9(4):597–612. https://doi.org/10.1007/s11440-013-0286-8.

[31] Tsinidis G, Pitilakis K, Trikalioti AD. Numerical simulation of round robin numerical test on tunnels using a simplified kinematic hardening model. Acta Geotech 2014;9(4):641–59. https://doi.org/10.1007/s11440-013-0293-9.
[32] Gomes RC. Numerical simulation of the seismic response of tunnels in sand with an elastoplastic model. Acta Geotechnica 2014;9(4):613–29. https://doi.org/10.1007/s11440-013-0287-7.
[33] Hleibieh J, Wegener D, Herle I. Numerical simulation of a tunnel surrounded by sand under earthquake using a hypoplastic model. Acta Geotechnica 2014;9(4):631–40. https://doi.org/10.1007/s11440-013-0294-8.
[34] Lanzano G, Bilotta E, Russo G, Silvestri F, Madabhushi SG. Centrifuge modeling of seismic loading on tunnels in sand. Geotech Test J 2012;35(6):854–69. https://doi.org/10.1520/GTJ104348.
[35] Wang JN. Seismic design of tunnels: a state-of-the-art approach. monograph, monograph 7. New York: Parsons, Brinckerhoff, Quade and Douglas Inc; 1993.
[36] Penzien J. Seismically induced racking of tunnel linings. Earthq Eng Struct Dynam 2000;29(5):683–91.
[37] Anastasopoulos I, Gazetas G. Analysis of cut-and-cover tunnels against large tectonic deformation. Bull Earthq Eng 2010;8(2):283–307. https://doi.org/10.1007/s10518-009-9135-4.
[38] Tsinidis G, Rovithis E, Pitilakis K, Chazelas JL. Seismic response of box-type tunnels in soft soil: experimental and numerical investigation. Tunn Undergr Space Technol 2016;59:199–214. https://doi.org/10.1016/j.tust.2016.07.008.
[39] McKenna F. OpenSees: a framework for earthquake engineering simulation. Comput Sci Eng 2011;13(4):58–66.
[40] Visone C, Santucci de Magistris F. Mechanical behaviour of the Leighton Buzzard Sand 100/170 under monotonic, cyclic and dynamic loading conditions. In: Anidis 2009 - XIII Convegno ANIDIS-L'ingegneria Sismica in Italia" in Bologna, Italy, 28 June -2 July; 2009.
[41] Mejia LH, Dawson EM. May). Earthquake deconvolution for FLAC. In: 4th International FLAC symposium on numerical modeling in geomechanics; 2006. p. 4–10.
[42] Thomas A. Sprayed Concrete Lined Tunnels. CRC Press; 2018. https://doi.org/10.1201/9781482265682.
[43] Yang Z, Elgamal A. Command Manual and User Reference for OpenSees Soil Models and Fully Coupled Element Developed at. San Diego: University of California at; 2003.
[44] Lanzano G, de Magistris FS, Bilotta E. Calibration of the mechanical parameters for the numerical simulations of dynamic centrifuge experiments. 2014. p. 169–74.
[45] Lyon B. Evaluación de Riesgo Sísmico de Túneles Circulares en Depósitos de Suelo (in Spanish) (M.Sc. Dissertation, Universidad del Desarrollo. Facultad de Ingeniería, Chile; Retrieved from, http://hdl.handle.net/11447/3229; 2019.
[46] Darandeli M. Development of a new family of normalized moduli reduction and material damping curves. Ph. D. Thesis]. Austin: University of Texas at Austin); 2001. Doctoral dissertation.
[47] Idriss IM, Seed HB. Seismic response of soil deposits. J Soil Mech Found Div 1970;96(2):631–8.
[48] Candia G, Macedo J, Jaimes MA, Magna-Verdugo C. A new state-of-the-art platform for probabilistic and deterministic seismic hazard assessment. Seismol Res Lett 2019;90(6):2262–75. https://doi.org/10.1785/0220190025.
[49] Kwong N Simon, Chopra Anil K. McGuire Tunnel performance during the Puebla-Mexico 19 September 2017 earthquake. Earthquake Spectra; 2017.
[50] Vamvatsikos D, Cornell CA. Incremental dynamic analysis. Earthq Eng Struct Dynam 2002;31(3):491–514. https://doi.org/10.1002/eqe.141.
[51] Azarbakht A, Dolšek M. Progressive incremental dynamic analysis for first-mode dominated structures. J Struct Eng 2011;137(3):445–55. https://doi.org/10.1061/(ASCE)ST.1943-541X.0000282.
[52] Araya-Letelier G, Parra PF, Lopez-Garcia D, Garcia-Valdes A, Candia G, Lagos R. Collapse risk assessment of a Chilean dual wall-frame reinforced concrete office building. Eng Struct 2019;183:770–9. https://doi.org/10.1016/j.engstruct.2019.01.006.
[53] Poulos A, Monsalve M, Zamora N, de la Llera JC. An updated recurrence model for Chilean subduction seismicity and statistical validation of its Poisson nature. Bull Seismol Soc Am 2019;109(1):66–74. https://doi.org/10.1785/0120170160.
[54] Strasser FO, Arango MC, Bommer JJ. Scaling of the source dimensions of interface and intraslab subduction-zone earthquakes with moment magnitude. Seismol Res Lett 2010;81(6):941–50. https://doi.org/10.1785/gssrl.81.6.941.
[55] Montalva GA, Bastías N, Rodriguez-Marek A. Ground-motion prediction equation for the Chilean subduction zone. Bull Seismol Soc Am 2017;107(2):901–11. https://doi.org/10.1785/0120160221.
[56] Abrahamson N, Gregor N, Addo K. BC Hydro ground motion prediction equations for subduction earthquakes. Earthq Spectra 2016;32(1):23–44. https://doi.org/10.1193/051712EQS188MR.
[57] Castro S, Benavente R, Crempien J, Candia G, de la Llera JC. A consistently processed strong motion database for Chilean earthquakes. Retrieved January 2020 from SIBER-RISK database, https://doi.org/10.7764/datasetUC/ING-UC.117 0836_1; 2021.
[58] Seed RB, Bray JD, Chang SW, Dickenson SE. Site-dependent seismic response including recent strong motion data. In: 14th International Conference on soil and Foundation engineering in Sitzungsberichte. 6; 1997. p. 125–34. 12 September, Hamburg, Germany.
[59] Anderson DG. Seismic Analysis and Design of Retaining Walls, Buried Structures, Slopes, and Embankments. Transportation Research Board; 2008.